

Detached Eclipsing Binaries in Compact Hierarchical Triples: Triple-lined systems BD+44 2258 and KIC 06525196

Ayush Moharana,^{1*} K. G. Helminiak,¹ F. Marcadon,^{1,2} T. Pawar,¹ M. Konacki,³ N. Ukita,^{4,5} E. Kambe,⁶ and H. Maehara⁴

¹*Nicolaus Copernicus Astronomical Center, Polish Academy of Sciences, ul. Rabiańska 8, 87-100 Toruń, Poland*

²*Villanova University, Dept. of Astrophysics and Planetary Sciences, 800 East Lancaster Avenue, Villanova, PA 19085, USA*

³*Nicolaus Copernicus Astronomical Center, Polish Academy of Sciences, ul. Bartycka 18, 00-716 Warszawa, Poland*

⁴*Okayama Astrophysical Observatory, National Astronomical Observatory of Japan, 3037-5 Honjo, Kamogata, Asakuchi, Okayama 719-0232, Japan*

⁵*The Graduate University for Advanced Studies, 2-21-1 Osawa, Mitaka, Tokyo 181-8588, Japan*

⁶*Subaru Telescope, National Astronomical Observatory of Japan, 650 North Aohoku Place, Hilo, HI 96720, USA*

Accepted XXX. Received YYY; in original form ZZZ

ABSTRACT

Compact Hierarchical Triples (CHT) are systems with the tertiary star orbiting the inner binary in an orbit shorter than 1000 days. CHT with an eclipsing binary as its inner binary can help us extract a multitude of information about all three stars in the system. In this study, we use independent observational techniques to estimate the orbital, stellar, and atmospheric parameters of two triple-lined CHT: BD+44 2258 and KIC 06525196. We find that the masses of stars in BD+44 2258 are $1.011 \pm 0.029 M_{\odot}$, $0.941 \pm 0.033 M_{\odot}$, and $0.907 \pm 0.065 M_{\odot}$ while in KIC 06525196 the estimated masses are $1.0351 \pm 0.0055 M_{\odot}$, $0.9712 \pm 0.0039 M_{\odot}$, and $0.777 \pm 0.012 M_{\odot}$. Using spectral disentangling, we obtained individual spectra of all the stars and combined it with light curve modelling to obtain radii, metallicities and temperatures. Using stellar evolution models from MESA, we constrain the $\log(\text{age})$ of BD+44 2258 to be 9.89 and 9.49 for KIC 06525196. Two stars in BD+44 2258 are found to be sub-giants while all three stars in KIC 06525196 are main-sequence stars. We constrain the mutual inclinations to certain angles for BD+44 2258 and KIC 06525196 using numerical integration. Integrating with tidal interaction schemes and stellar evolution models, we find that KIC 06525196 is a stable system. But the inner binary of BD+44 2258 merges within 550 Myrs. The time of this merger is affected by the orientation of the tertiary, even rushing the collapse by ~ 100 Myrs when the mutual inclination is close to 90 degrees.

Key words: binaries: eclipsing – binaries: spectroscopic – stars: fundamental parameters – stars: evolution – stars: individual: BD+44 2258, KIC 06525196 – stars: kinematics and dynamics

1 INTRODUCTION

The multiplicity of stars is a well-established phenomenon (Duchêne & Kraus 2013). The incidence of multiplicity varies with the spectral type of the stars. Multiplicity is 44% among the Solar-like stars, out of which 8% are triple stars (Raghavan et al. 2010). These numbers increase in O, B, and A types (Mason et al. 2009; Shatsky & Tokovinin 2002; Kobulnicky & Fryer 2007). There have been a lot of studies towards understanding binaries which has created an almost complete picture of their evolution and formation. The next step in decoding the multiple-architecture is understanding triple systems.

Binary formation channels can be largely classified into disk instability, core-fragmentation, and N-body interactions. The complexity of formation increases in a triple system with a combination of these formation channels being responsible for their formation (Tokovinin 2021). Most of the studies to understand these scenarios using orbital architectures, metallicity variation among stars, and mass distribu-

tions in triples, have been usually restricted to wide triples (Tokovinin 2017, 2022; Lee et al. 2019).

The evolution of triple stars also departs from the simplified evolution of a single star. A triple-star system has the additional complexity of multiple dynamical interactions. The outer companion can directly alter the formation of the components of the inner binary, leading to their apparent difference in properties (e.g. apparent age; Marcadon et al. 2020), and has been used in explaining various evolutionary phenomena of single and binary stars.

Hierarchical triple systems have been intensely studied in order to understand the formation of closest main-sequence binary systems (Eggleton & Kiseleva-Eggleton 2001; Naoz & Fabrycky 2014; Moe & Kratter 2018). One of the probable theories of the formation of blue straggler stars involves perturbations from a third body (Perets & Fabrycky 2009). One in a thousand high-mass x-ray binaries evolve through interaction with a third star to form low-mass x-ray binaries (Eggleton & Verbunt 1986). Asymmetry of Planetary Nebulae has been linked to evolution in a triple system (Akashi & Soker 2017; Jones et al. 2019) and has even been suspected to play a role in

* E-mail: ayushm@ncac.torun.pl

driving white dwarf mergers towards type Ia supernova explosions (Maaz et al. 2014).

Recent population synthesis studies have shown that 65–75 % of triples undergo mass transfer (Toonen et al. 2020). Hamers & Dosopoulou (2019) have shown that this can occur uniformly throughout the orbit or at certain points due to eccentricity and inclination changes known as von Zeipel-Lidov-Kozai (ZLK) oscillations (von Zeipel 1910; Lidov 1962; Kozai 1962). Furthermore, these systems perturb Roche-lobe potentials and also undergo Roche-Lobe Over Flow (RLOF), which can occur for the three individual stars and can be circumbinary too. Therefore, understanding the stellar evolution coupled with the dynamical evolution is important when studying triples. Most of the known triple systems have long tertiary periods and therefore their dynamical effects can have timescales of decades or centuries. There is a subset of these triples, called Compact Hierarchical Triples (CHT), which offer more potential for observational astrophysics (Borkovits 2022). The timescale of the changes due to these interactions is short in CHT and can be observed easily over a few years, e.g., vanishing eclipses of HS Hya (Zasche & Paschke 2012) or re-appearing eclipses of V907 Sco (Zasche et al. 2023). These are triples with the outer orbit period shorter than 1000 days. Due to this, dynamical processes in CHTs can be observed in timescales of years. CHTs were thought to be rare (Tokovinin 2004) but with new space-based photometric missions we are discovering more of these systems (Rappaport et al. 2013; Borkovits et al. 2016).

Detached Eclipsing Binaries (DEB) are known as the source of the most accurate stellar parameters (e.g., mass, radius, etc.). Accuracy of less than 1% can be attained by coupling high-precision photometry and high-resolution spectroscopy (Torres et al. 2010). The accuracy is robust and independent of different models and methods, even varying slightly due to different numerical implementations (Maxted et al. 2020; Korh et al. 2021).

If a CHT has a DEB as its inner binary, there is an added advantage of obtaining accurate stellar parameters of not only the binary but of the tertiary as well (Helminiak et al. 2017). Using light curve modelling, eclipse timing Variations, spectral analysis, and RVs, we can obtain an accurate picture of the orbits, geometry, stellar parameters, metallicity, age, and evolutionary status.

There has been a surge in interest in CHT recently. *Kepler* (Howell et al. 2014) and Transiting Exoplanet Survey Satellite (*TESS*) both have been crucial in detection and analysis of these systems (Borkovits et al. 2015, 2020). Tertiary stars in CHT have been found to host tidally induced pulsations (Fuller et al. 2013). Ongoing projects are using triply-eclipsing triples (TET) to characterise CHT (Rappaport et al. 2022). Studies even show that CHT can produce exotic Thorne-Żytkow objects (Eisner et al. 2022). Last but not the least, CHT have proven to be useful to study ZLK oscillations and their effect on stellar evolution (Borkovits et al. 2022). Though most of these studies have provided us with mass and radii of all the stars in a CHT, the tertiary radii-space is dominated by TET or planar systems.

In this paper, we report the detection of a DEB in a CHT, BD+44 2258 ($\alpha = 13:15:06.66$, $\delta = 44:02:33.48$; hereafter BD44). BD44 has been previously observed in UV (GALEX; Bianchi et al. 2011) and X-Ray (ROSAT; Voges et al. 1999) but as a single source. We obtain stellar, orbital, and atmospheric parameters of all the stars in BD44 and a previously detected CHT, KIC 06525196 ($\alpha = 19:30:52.32$, $\delta = 41:55:20.81$; hereafter KIC65) with *TESS* photometry and HIDES spectroscopy. We explain the different observations and methods used for extracting parameters in Sections 2 and 3. We use these parameters to estimate the age and evolutionary stages of the components. Further, using the orbital parameters, we study the evolution and stability of the systems as explained in Section 4.

2 OBSERVATIONS

2.1 Photometry

We use photometry from *TESS* (Ricker et al. 2015) for our light curves¹(LC). BD44 (TIC 284595199) has 2-minute cadence photometry obtained from Sectors 16, 22, and 49. KIC65 was a target from the main *Kepler* mission field, and these data have been analysed in Helminiak et al. (2017). In addition to this, the *TESS* 2-minute cadence photometry (TIC 137757776) is available from Sectors 40 and 41. In this work, we only model a segment of *TESS* data from Sector 41 for KIC65 while for BD44 we use segments from Sectors 16, 22, and 49. These segments were selected on the basis of spot variability in the LCs. This was also the reason for selecting only Sector 41 for KIC65 because the overall structure of the LC was similar in both sectors but Sector 41 has fewer fluctuations than Sector 40. The structure of the LC for BD44 changes in the sectors and therefore we model all the sectors to check for consistency.

We filtered out the points which had the best quality-flag for our purposes. There seems to be no other star in the Full Frame Image of BD44 but there seems to be some contamination for KIC65. For BD44, we compared normalised LCs obtained using different apertures on the FFIs only to find they all are identical when normalised. Therefore we consider that any third light that would show up from LC modelling will be solely due to the third star. We considered the Simple Added Photometry or SAP fluxes for modelling both our systems.

2.2 Spectroscopy

We use spectra collected with the HIDES (Izumiura 1999; Kambe et al. 2013), attached to the 1.88-m telescope at the Okayama Astrophysical Observatory. Observations were conducted in the fiber mode with an image slicer ($R \sim 50\,000$), without I_2 , and with ThAr lamp frames taken every 1–2 hours. The spectra are composed of 62 rows covering 4080–7538 Å, of which we use 30 (4365–6440 Å) for radial velocity (RV) calculations. A detailed description of the observing procedure, data reduction and calibrations is presented in Helminiak et al. (2016).

For KIC65 we used exactly the same set of 14 spectra and RV measurements as in Helminiak et al. (2017). For BD44 we took a total of 28 spectra.

3 ANALYSIS

In the following sections, we use A-B notation to denote the CHT, where B is the tertiary. A is the eclipsing binary with components Aa and Ab. Aa corresponds to the primary classified according to temperature, usually the deepest eclipse in the LC if not affected by spots. Since we would be talking about six stars in total (three in each of the two CHT), we use the short form for the star's name along with the alphabetical notation to exclusively denote each star, e.g., the secondary (cooler star in the binary) of KIC65 is referred as KIC65Ab.

3.1 RV extraction and fitting

Since both targets were observed with the same spectrograph as part of the same programme, the approach to RV calculations and fitting

¹ From GI programmes: G022003, G022062, G04047, G04171, G04234.

was essentially identical. It is described in detail in Helminiak et al. (2017), but we summarise it here briefly.

The RVs were calculated with a TODCOR method (Zucker & Mazeh 1994) with synthetic spectra computed with ATLAS9 code as templates. Measurement errors were calculated with a bootstrap approach and used for weighting the measurements during the orbital fit, as they are sensitive to the signal-to-noise ratio (SNR) of the spectra and rotational broadening of the lines. Though this code is optimised for double-lined spectroscopic binaries and provides velocities for two stars (u_1, u_2), it can still be used in triple-lined systems as well. The RVs of the eclipsing pair were found from the global maximum of the TODCOR map since in both targets these components contribute more to the total flux than the third star. The tertiary's velocities were found from a local maximum, where u_1 was set for the tertiary, and u_2 for the brighter component of the eclipsing pair. This scheme was used previously for KIC65 in Helminiak et al. (2017), and the *rms* of the resulting tertiary's RVs was comparable to the stability of the instrument estimated from RV standard stars. In some cases, the velocity difference between two components was too small to securely extract their individual RVs, and measurements were taken only for the remaining one. For this reason, each component of a given triple may have a different number of RV data.

The orbital solutions were found using our own procedure called v2FIT (Konacki et al. 2010). It applies a Levenberg-Marquardt minimisation scheme to find orbital parameters of a double-Keplerian orbit, which can optionally be perturbed by a number of effects, like a circumbinary body. The fitted parameters are: orbital period P , zero-phase T_P^2 , systemic velocity γ , velocity semi-amplitudes $K_{1,2}$, eccentricity e and periastron longitude ω , although in the final runs, the last two parameters were usually kept fixed to zero. We also included the difference between systemic velocities of two components, $\gamma_2 - \gamma_1$, and a circumbinary body on an outer orbit, parameterised analogously by orbital parameters P_3, T_3, K_3, e_3 , and ω_3 . In such case, γ is defined in the code as the systemic velocity of the whole triple.

Systematic errors that come from fixing a certain parameter in the fit are assessed by a Monte-Carlo procedure, and other possible systematics (like coming from poor sampling, small number of measurements, pulsations, etc.) by bootstrap analysis. All the uncertainties of orbital parameters given in this work already include the systematics.

In addition, for each observation where three sets of lines were sufficiently separated, we also calculated the systemic velocities $\gamma(t_i)$ of the inner pair, using the formula:

$$\gamma(t_i) = \frac{v_1(t_i) + qv_2(t_i)}{1 + q}, \quad (1)$$

where $v_{1,2}(t_i)$ are the measured RVs of the inner binary, and q is the mass ratio, found from the RV fit with a circumbinary perturbation. With these values as the center-of-mass (COM) RVs of the binary and RVs of the tertiary component, we can treat the long-period outer orbit as an SB2 (Fig.1), and independently look for its parameters. The final values of P_3, K_3, e_3 , etc., actually come from such fits.

3.2 Broadening Functions

Broadening function (BF) is a representation of the spectral profiles in velocity space. BF contains the signature of the RV shifts of different

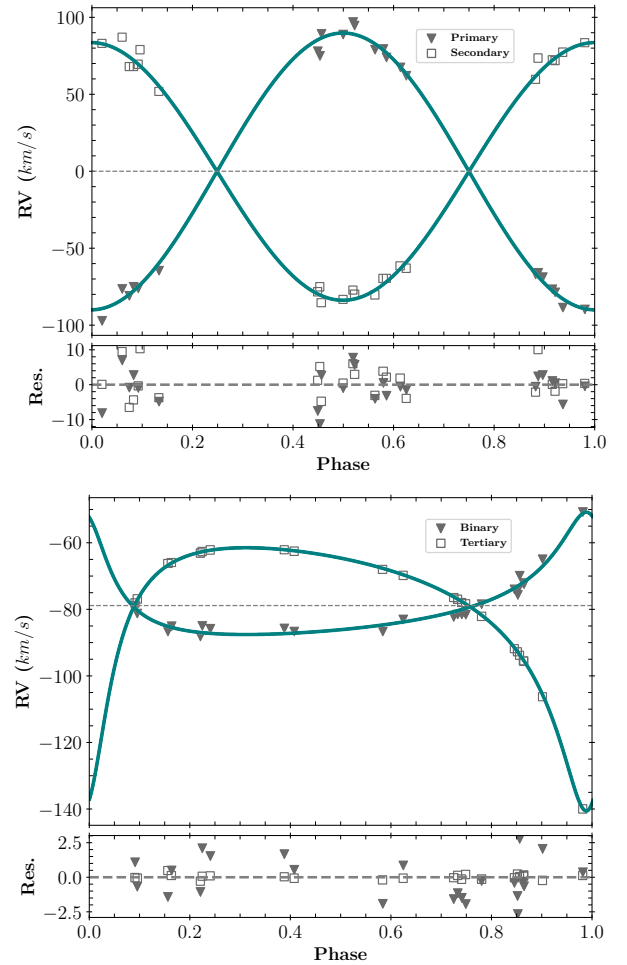


Figure 1. Phased RV profiles of BD44, for the inner binary (top) and the whole system (COM of the binary vs the tertiary). The green lines are the best v2FIT models. Though the tertiary has a good fit, the residuals from the binary fit contribute to the final uncertainties in the tertiary parameters.

lines and also intrinsic stellar effects like rotational broadening, spots, pulsations, etc (Rucinski 1999a). The BF was calculated using the algorithm described in Rucinski (1999b). We modified a single-order BF code, BF-RVLOTTER³, to calculate multi-order BF and also fit the function with multiple Gaussian or rotation functions. The BF was calculated in a wavelength range of 5050-5600 Å. We used a synthetic solar-type spectrum with zero projected rotational velocity ($v \sin(i)$) as our template. The final BF generated was smoothed with a Gaussian smoother of a 3 km s^{-1} rolling-window. Three clear peaks were visible in all epochs of spectra which implied that we did not observe the system spectra during eclipses of any of the three stars. The peaks were fitted with the rotational profile from Gray (2005),

$$G(v) = A \left[c_1 \sqrt{1 - \left(\frac{v}{v_{\max}} \right)^2} + c_2 \left(1 - \left(\frac{v}{v_{\max}} \right)^2 \right) \right] + lv + k \quad (2)$$

where A is the area under the profile and v_{\max} is the maximum velocity shift that occurs at the equator. c_1 and c_2 are constants that are a function of limb darkening themselves while l and k are correction factors to the BF "continuum". The fits revealed distortions

² Defined as the moment of passing the pericentre for eccentric orbits or quadrature for circular.

³ <https://github.com/mrawls/BF-rvplotter>

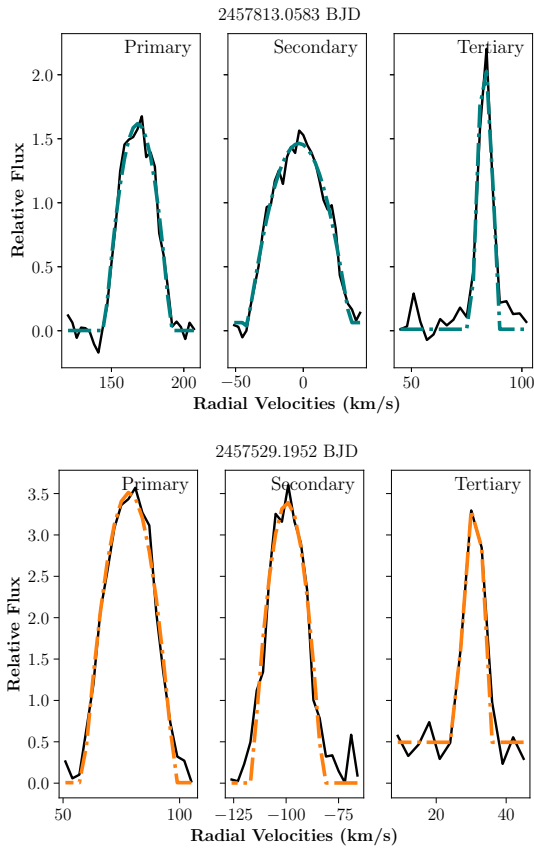


Figure 2. Broadening functions for all the three components of BD44 (top) and KIC65 (bottom). The green and orange dashed line represents best-fit rotational profile for BD44 and KIC65 respectively. The sharp kinks or distortions on the BF peaks are most likely due to spots.

(sharp kinks) of the BF from the ideal rotational profiles (Fig. 2). These are most likely due to spots, and this gives us a qualitative idea about the relative number of spots on the stars. These fits for different epochs were used to (i) calculate light contributions (the parameter A) from different companions, and (ii) make an initial estimate of $v \sin(i)$ (the parameter v_{\max}) for spectral analysis. We also used BF to calculate RVs and found them consistent with the TODCOR RVs. Therefore, for the sake of consistency and familiarity, we used RVs from TODCOR.

3.3 Spectral Disentangling

A detailed study of stellar evolution needs a model-independent estimate of stellar metallicity. To estimate atmospheric parameters and abundances, we need spectra for all three stars in the CHT. We use the technique of Spectra Disentangling (hereafter: *SPD*; Simon & Sturm 1994; Hadrava 1995), for separating individual spectra of the component stars from the composite spectra. This method, though, takes in the assumption that the line profiles are not intrinsically variable. This would mean that we should consider only the out-of-eclipse spectra so as to avoid such variability during the eclipse (e.g., Rossiter-McLaughlin effect). One of the advantages of this method is that it can detect faint companions, i.e., $< 3\%$ light contribution (Holmgren et al. 1999; Mayer et al. 2013). This, though, requires good phase coverage and high signal-to-noise ratio.

For our purpose, we used a python-based wrapper⁴ around the disentangling code *FDBINARY* (Ilijic et al. 2004), which can disentangle up to three components. The wrapper takes two inputs: (i) an estimate of orbital parameters and (ii) RV corrections and light-ratios at each epoch of spectra used from disentangling. We used the solution from RV fitting as starting values in our optimisation. The light-ratios at every epoch were calculated from the BFs. To make the computation easy and avoid any wavelength dependency, we divided the total spectral range into four sections with overlapping regions. The final disentangled spectra were stitched after normalisation, and removal of the edges of the segmented-disentangled spectra. The overlapping regions acted as check-points for normalisation as they helped us choose the normalisation function which gave the same line-depths for a particular, overlapping spectral line. The errors of the disentangled spectra were taken as the sum of errors calculated from SNR, and flux-scaled residuals from the disentangled routine.

3.4 Light curve fitting

We use the version 4 of *PHOEBE 2* code⁵ (Prša et al. 2016; Horvat et al. 2018; Jones et al. 2020; Conroy et al. 2020) for our LC modelling. *PHOEBE 2* models eclipsing binaries (or single stars) by discretising the surface of each star. It also distorts the stellar surfaces according to their Roche potentials. The key feature that made us choose this code is its ability to model spots and also solve the inverse problem with spot parameters free for optimisation.

The first look on the LCs of BD44 and KIC65 suggests the presence of cold spots in the stars. Comparing the light-curve of the different sectors reveals that the spots are time-evolving. We, therefore, approach our modelling by dividing the light-curve into segments with relatively-stable spot signatures. While we model all available sectors for BD44 (Fig. 3), we only model only Sector-41 for KIC65 (Fig. 4). Further, the distortions on the BF suggest the secondary to be more active than the primary for both stars. Therefore, in our models, we assume more spot(s) on the secondary than the primary. The third-light (l_3) is expected in a triple-lined CHT unless the signatures are removed with detrending methods. The l_3 is highly degenerate with the inclination (i) too. Estimating l_3 for our systems, from LC, adds another level of complexity with the cold spots affecting the depths of the eclipse. We assume that the values of light-fractions obtained from BF of optical spectra are similar to the light-fraction of the components in the *TESS* band. Therefore, we start with an initial l_3 equal to the flux-fraction of the tertiary from BFs.

Considering the above assumptions and fixing parameters obtained from RV fitting, i.e., mass-ratio (q), semi-major axis (a), and period of the binary (P_b), we used *lc_geometry* estimator in *PHOEBE 2* for initial parameter estimates. We then added spots one by one and minimising overall trends in the residuals manually. We added 1 spot on the secondary of KIC65 and stopped at three spots (2 on secondary, 1 on primary) for BD44. More spots would have compromised our computational resources. We then optimised for stellar parameters using Nelder-Mead (Nelder & Mead 1965) optimisation module in *PHOEBE 2*. The optimised parameters include radii of primary and secondary (R_{Aa} and R_{Ab} respectively), time of super-conjunction (T_0), ratio of secondary temperature to the primary temperature (T_{ratio}), P_A , l_3 , i_A , and passband luminosity of the primary (L_{Aa}). Since the RV fitting didn't show any substantial eccentricity for the binary (e_A), we kept it fixed at zero which also reduced the computational

⁴ https://github.com/ayushmoharana/fd3_initiator

⁵ <http://phoebe-project.org/>

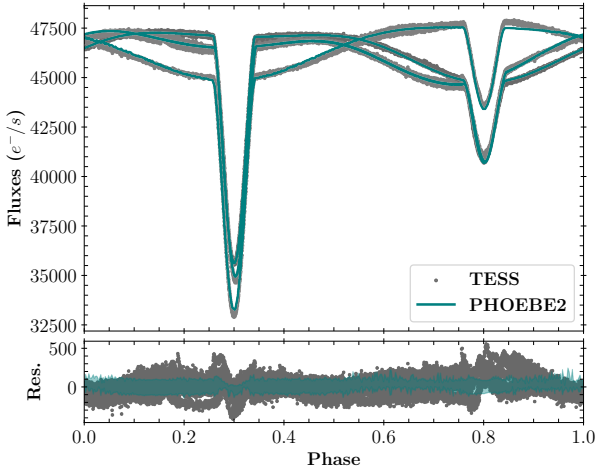


Figure 3. Phased TESS LC (for stable segments from all sectors) for BD44. The green lines represent best-fit PHOEBE 2 model. The shaded areas are translated from the adopted errors of the MCMC solution from Sector-16.

cost. After minimising the residuals below 1% of the total flux, we optimised for all spot parameters (co-latitude⁶ c^{spot} , longitude l^{spot} , relative-temperature T^{spot} , and radius r^{spot}) for all the three spots. We then randomly optimised, combinations of spot parameters and stellar parameters, to check the robustness of the optimisation.

We calculated the errors through the Monte Carlo Markov Chain (MCMC) sampling, implemented in EMCEE (Foreman-Mackey et al. 2013, 2019) and available as a sampler in PHOEBE 2. We decided on 8 parameters to be sampled including the relative temperature of the biggest spot in both the systems (T_{Ab}^{spot}). Due to the lack of computational resources, our initial sampling consisted of 40 walkers and was sampled till we got stable chains for 1000 iterations. Then we started from this sample-space and ran another sampling for 3500 stable chains with 80 walkers. To further check the convergence, we use auto-correlation plots (Box & Jenkins 1976) with Bartlett’s formula (Francq & Zakoian 2009) to find the minimum limit for auto-correlated chains. The uncertainties represent 68.27% confidence interval. To validate our results, we translated the errors on the light curves and also the residuals (Fig. 3 and 4).

3.5 Spectroscopic Analysis

We used iSPEC (Blanco-Cuaresma et al. 2014; Blanco-Cuaresma 2019) for spectroscopic analysis. Before the analysis, we prepared the spectra by correcting the RV offsets that was present in the SPD products. We fitted and corrected the continuum for the SPD spectra using a spline function of degree 3, consisting of 30-150 splines, depending on the component. We used the synthetic spectral fitting (SSF) method where iSPEC generates synthetic spectra on the go for the fitting. We used line masks for specific regions, generated by the spectral synthesis code SPECTRUM⁷ to calculate the χ^2 . The regions were generated on the line lists from Gaia-ESO Survey (GES; Gilmore et al. 2012; Randich et al. 2013) version 5.0 which covers the wavelength range of 420nm-920nm. There are two sets of GES line lists available in iSPEC, which we use: (i) list for abundances estimates (LL_a) and (ii) list for parameter estimate (LL_p). The spectral

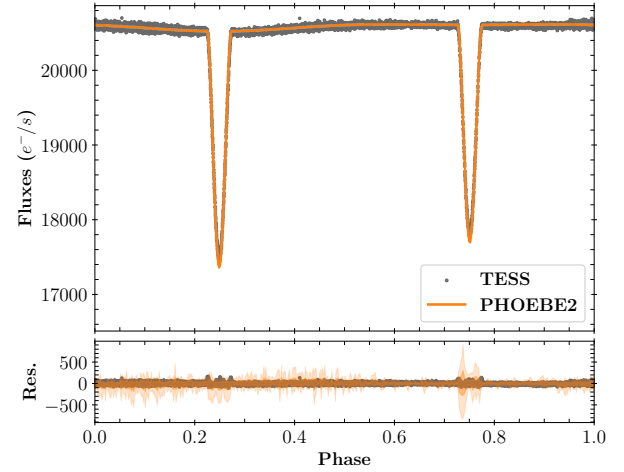


Figure 4. Phased TESS LC for KIC65. The orange lines represent best-fit PHOEBE 2 model. The shaded areas are translated from the adopted errors of the MCMC solution from Sector-41.

synthesis was again done using SPECTRUM with model atmospheres from Gustafsson et al. (2008). The solar abundances were chosen from Grevesse et al. (2007). In our initial test runs, with all parameters free, we found that the $v \sin i$ values were consistent with the values obtained from BFs. Therefore in our further runs, we fixed the respective $v \sin i$ for the components. Using LL_a, we did a search for metallicity, [M/H], on all three stars of the two CHT. Since the [M/H] of the stars of the respective CHT were consistent within the uncertainty range, we averaged the [M/H] estimates for the system and fixed it for further runs. In the final runs, we fixed the $\log(g)$ (obtained from LC models) for primary and secondary. The limb darkening coefficient (values were taken from Claret & Bloemen 2011) and resolution were kept fixed while marco-turbulence velocity was calculated automatically from an empirical relation established by GES and built in the code. For the estimation of temperatures (and $\log(g)$ for the tertiary), we selected only the part of the spectra with SNR of more than 40 (more than 18 for the tertiary). We chose LL_p for this fitting. The best fit synthetic spectra for all the stars in the study are shown in Fig. 7. We also calculated the radii R (in R_{\odot}) of the tertiary stars using $\log(g)$ (in dex) from spectra, by applying the formula:

$$R = A_c \sqrt{\frac{M}{10^{\log(g)}}}, \quad (3)$$

where M is the mass of the tertiary calculated from LC and RV fitting (in M_{\odot}) and $A_c \equiv \sqrt{GM_{\odot}/R_{\odot}}$ ($= 168.589888477$) is a constant necessary for transformation to solar units.

We calculated the α -enhancement with LL_a and fixed the rest of the parameters as given in Table. 1. Using this setup, the abundances⁸ were calculated using the SSF method but with free abundance and [M/H] for a particular element. We did not consider the abundances of the elements where we got large errors and/or where [M/H] was out of the pre-calculated bounds.

⁸ The abundances were obtained in the 12-scale as $A(X)$, where, $A(X) = \log\left(\frac{n_X}{n_H}\right) + 12$, in which n_X and n_H are the number of atoms of the element X and of hydrogen, respectively.

⁶ Co-latitude is measured along the spin axis with the North pole as 0° .

⁷ <http://www.appstate.edu/~grayro/spectrum/spectrum.html>

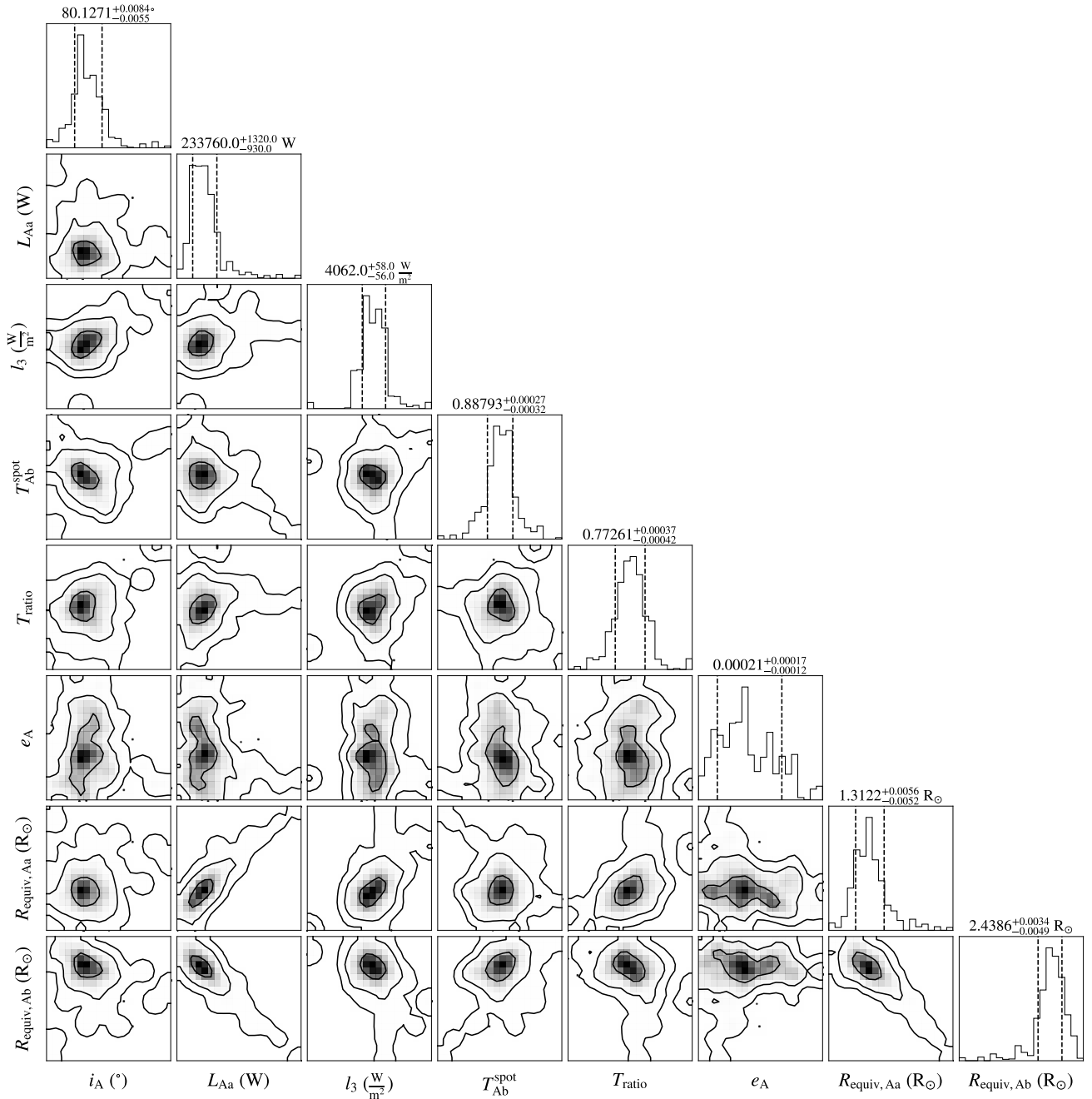


Figure 5. Corner plot for MCMC parameters from LC fitting of BD44. The contours on the maps correspond to 1σ , 2σ , and 3σ errors on the distribution. The effect of spots is visible in the distorted maps of the eccentricity parameter-space.

3.6 Isochrone Fitting

The age of each system was estimated with a grid of isochrones generated using a dedicated web interface,⁹ based on the Modules for Experiments in Stellar Astrophysics (MESA; Paxton et al. 2011, 2013, 2015, 2018), and developed as part of the MESA Isochrones and Stellar Tracks project (MIST v1.2; Choi et al. 2016; Dotter 2016).

The grid was prepared for iron abundance, $[\text{Fe}/\text{H}]$ ¹⁰, values from -4.0 to 0.50 dex with 0.05 dex steps, as well as for ages $10^{8.6}$ to $10^{10.2}$ Gyr, in logarithmic scale, every $\log(\text{age})=0.01$.

On each isochrone we were looking for a triplet of points that simultaneously best reproduce the observed values of any selected parameters from the following: masses $M_{1,2,3}$, radii $R_{1,2,3}$, and ef-

¹⁰ It is reasonable to assume that without significant deviations from solar amounts of α -elements, the iron abundance $[\text{Fe}/\text{H}]$ sufficiently approximates the amount of metals $[\text{M}/\text{H}]$.

⁹ <http://waps.cfa.harvard.edu/MIST/>

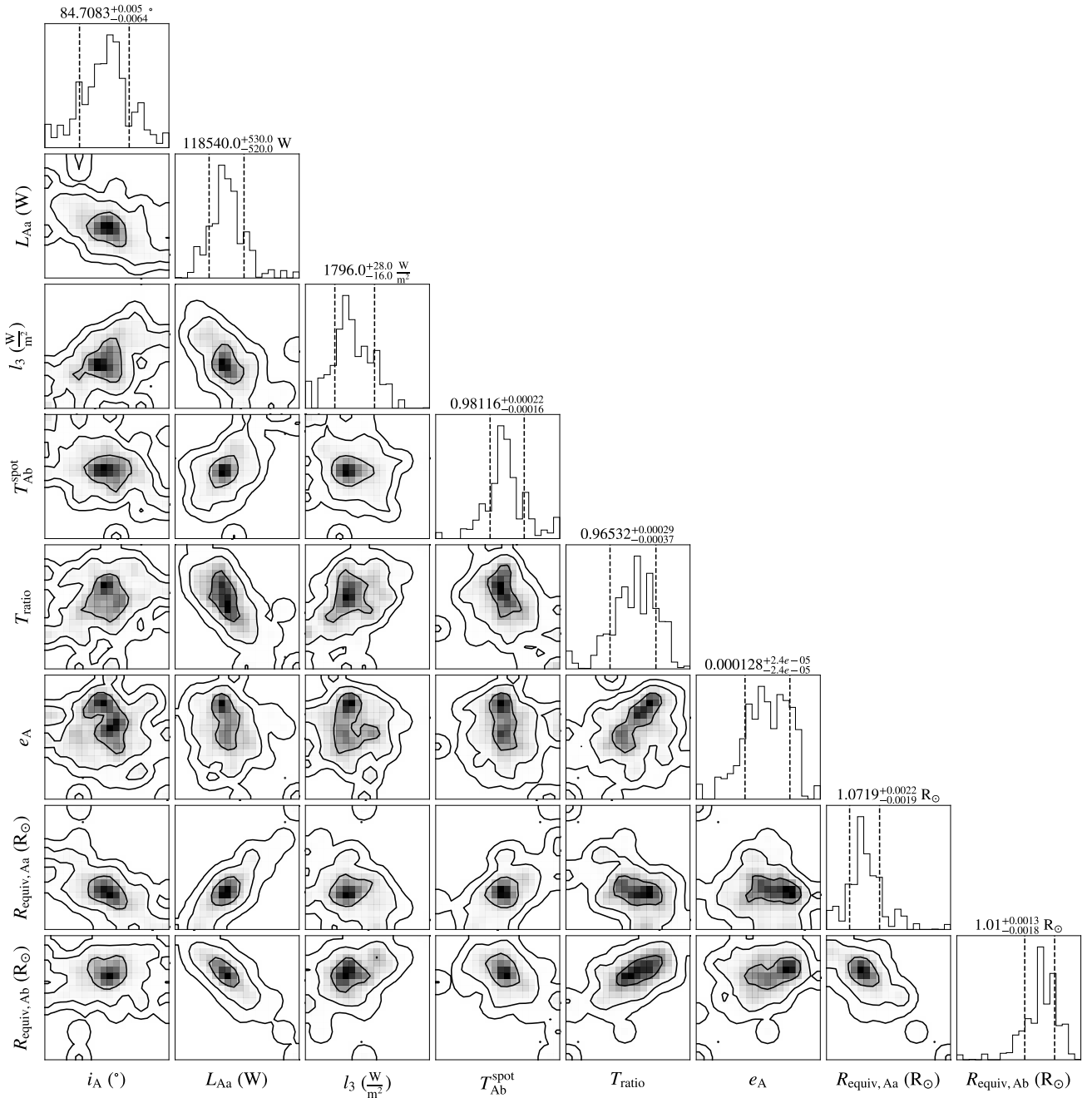


Figure 6. Corner plot for MCMC parameters from LC fitting of KIC65. The contours on the maps correspond to 1σ , 2σ , and 3σ errors on the distribution. The effect of spots is visible in the distorted maps of the eccentricity parameter-space. Also note that the distortion of the radii parameter-space is smaller than that of BD44.

fective temperatures $T_{1,2,3}^{\text{eff}}$ of three components, flux ratio of the inner binary’s components l_2/l_1 in the given band, as well as the $[\text{Fe}/\text{H}]$, and distance d . The method of simultaneously obtaining distances and reddening $E(B - V)$ reproduced by a given model (triplet of points on an isochrone) is described in Appendix A, as well as in Helminiak et al. (2021). In the recent 3rd *Gaia* Data Release (GDR3; Gaia Collaboration et al. 2022), solutions from the *Part 1. Main Source* have high value of the RUWE parameter (~ 2.6), and better solutions, with significantly different distances, are presented

in *Part 3. Non-single stars*. We used the latter ones as the constraints in our isochrone fitting.

It is worth noting that the *ISPEC* value of $[\text{M}/\text{H}]$ was also used as a constraint, and the “best-fitting” $[\text{Fe}/\text{H}]$ was searched for in the fitting process. For this reason, the values of $[\text{Fe}/\text{H}]$ (assumed equivalent to $[\text{M}/\text{H}]$, since $[\alpha/\text{Fe}] = 0$) may not be the same as $[\text{M}/\text{H}]$ found from spectra. In the literature, isochrone or evolutionary track fitting is often made under the assumption of fixed $[\text{M}/\text{H}]$. We find this approach incorrect.

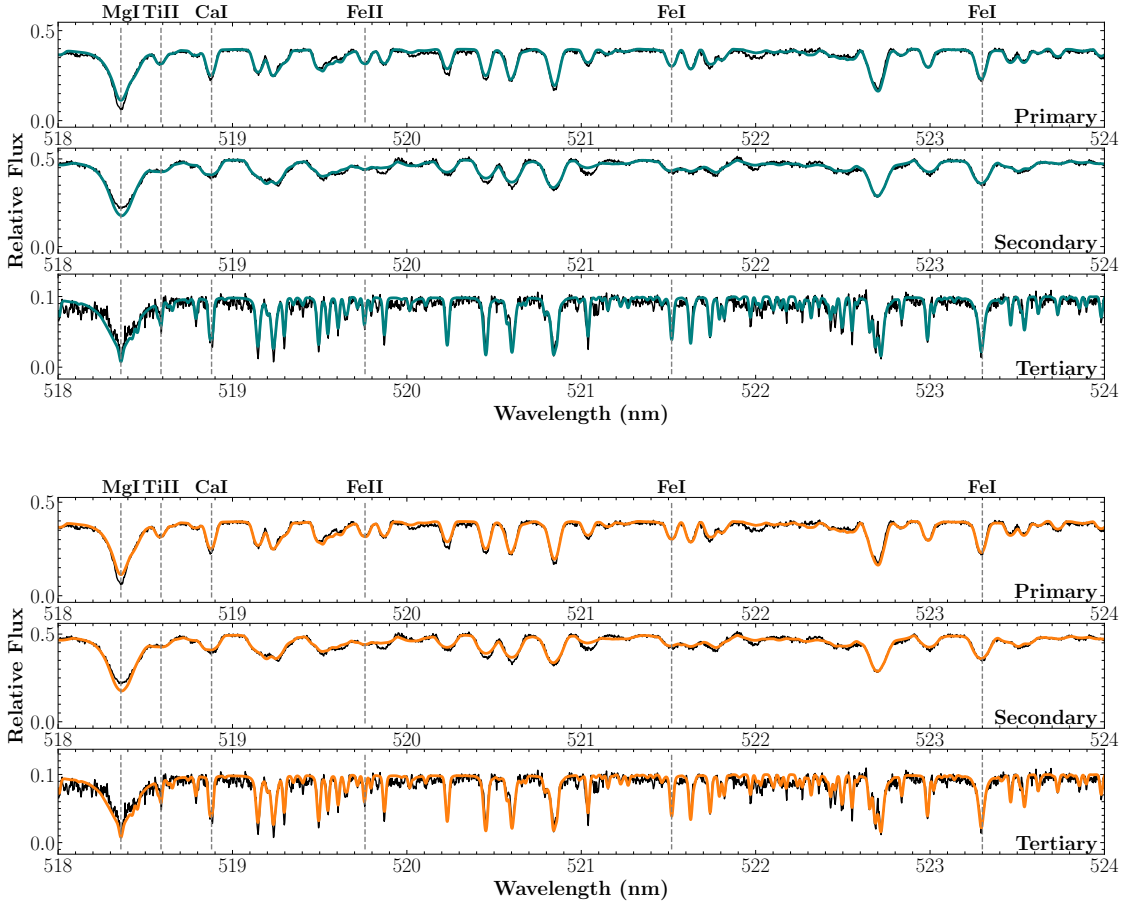


Figure 7. A section of the disentangled spectra and the best-fit synthetic template of all the components of BD44 (top) and KIC65 (bottom). The fit was obtained through the SSF method available in *iSpec*. While the SNR of the primary and secondary vary between 50-60, the tertiary component has a SNR ~ 18 . The section contains one of the wings of the Mg triplet and several Fe lines.

3.7 Numerical Integration of Orbital Dynamics

The accurate orbital parameters obtained enable us to probe the significant dynamical changes in these compact systems. The major orbital parameters that drive the dynamics are usually the masses, semi-major axes or periods, and all inclinations, including mutual inclination (i_m). While we get almost all orbital parameters from combined LC and RV analysis, we still lack the information about the longitude of ascending nodes (Ω_A and Ω_{AB} for inner and outer orbit respectively) and i_m . An estimate of the range of the i_m can be calculated from the constraints arising due to geometry, using i_A and i_{AB} . Simplifying the calculations from [Gronchi & Tommei \(2007\)](#) we get,

$$\cos i_m = \cos(\Omega_A - \Omega_{AB}) \times \sin i_A \sin i_{AB} + \cos i_A \cos i_{AB} \quad (4)$$

Since the value of $\cos(\Omega_A - \Omega_{AB})$ can vary between -1 and 1, we estimate the range of $\cos i_m$ to be,

$$\cos i_m \geq \cos i_A \cos i_{AB} - \sin i_A \sin i_{AB} \quad (5)$$

$$\cos i_m \leq \cos i_A \cos i_{AB} + \sin i_A \sin i_{AB} \quad (6)$$

Using trigonometric identities, we get the range of i_m to be,

$$i_A - i_{AB} \leq i_m \leq i_A + i_{AB} \quad (7)$$

This is the solution when the cosine of i_m is positive (say configuration A). There exists another set of solution for a negative cosine configuration (say configuration B),

$$180 - (i_A + i_{AB}) \leq i_m \leq 180 - (i_A - i_{AB}) \quad (8)$$

This gives us a range of $0^\circ - 169.4^\circ$ (for Config.A) or $10.6^\circ - 180^\circ$ (Config.B) for the i_m of KIC65. While for BD44, we get a range of $3.98^\circ - 156.27^\circ$ (Config.A) or $23.73^\circ - 176.02^\circ$ (Config.B). To further constrain this range, we rule out the unrealistic i_m by looking at average i_A variations in the numerical integration of orbital parameters, and comparing with the i_A from the observations. For our work, we use [REBOUND¹¹](#), an open-source collisional N-body code ([Rein & Liu 2012](#)). REBOUND can also be used to simulate collision-less problems such as the three-body hierarchical orbit in our case. We use the symplectic integrator [WHFAST](#) which is designed for long-term integration of gravitational orbits ([Rein & Tamayo 2015](#)). WHFAST uses mixed-variables (Jacobi and Cartesian) and also a symplectic corrector which ensures accurate and fast integration of the N-body dynamical equations. The general setup is defined by masses and orbital parameters obtained with our observations. The

¹¹ <https://github.com/hannorein/rebound>

values of inclinations, ω and other orientation parameters are also taken from our observations (Table.1). Further, we use the REBOUNDX (Tamayo et al. 2020) library for adding in tidal forces and dissipation to this setup. The implementation uses a constant time-lag model from (Hut 1981) to raise tides on the larger (and more massive) stars. The constant time-lag parameter (τ) is given by,

$$\tau = \frac{2R^3}{GMt_f} \quad (9)$$

where R , M are the radius and mass of the body with tides (BD44Ab and KIC65Aa in our case) and t_f is convective friction time which is assumed as 1yr as described in REBOUNDX setup¹². G is the gravitational constant. The other inputs from observations include the rotation frequency of the secondary and its radius. The tidal Love number of degree 2 (tctlk2) is assumed to be 0.01. Using this setup, we simulate the systems for a time equal to the time between the observation of the first and last LC of the corresponding systems, i.e., 2.7yrs for BD44 and 6.9yrs for KIC65. We track the inclination changes of the inner binary for different values of Ω_{AB} (and assuming $\Omega_A = 0^\circ$) and then compare it with the observations.

A long-term look at such close systems ($P_A \sim 3d$) would require a coupled stellar evolution and dynamical evolution treatment. For this, we use the parameter-interpolation module in REBOUNDX. We update the radius and masses in the numerical simulation from MIST evolutionary tracks for the tidal stars (BD44Ab and KIC65Aa) in the inner binary. We start with an integration timestep of 1/30 times the inner binary period but update the integration timestep, if the orbit shrinks, so that we can track close encounters or collisions. With this setup, we simulate our systems for 600 Myrs.

4 RESULTS AND DISCUSSION

4.1 Physical parameters of the Binary

The binary components of the two systems are found to be of similar orbital configurations. This gives us an interesting case of comparing the effect of the tertiary on the binary system. The inner mass-ratio of BD44 is 0.931 (or 1/1.074) while for KIC65 it is 0.9383. The corresponding inner orbit periods of BD44 and KIC65 are 3.4726217d and 3.4205977d, respectively. The differences in the binaries of the two systems appear when we look at the LC solutions. The radius of the most massive star in BD44 is larger ($R_{Ab} = 2.4387^{+0.0035}_{-0.0048} R_\odot$) but it corresponds to the secondary (shallower) eclipse in the LC. This is also evident from the light-fractions obtained from the BF and also the fast rotation as reflected in the high $v\sin(i)$. Going by the convention, we will address this star as the secondary (BD44Ab; thus the secondary-to-primary mass ratio is >1). The primary of BD44 (BD44Aa) is inflated compared to the solar radius ($R_{Aa} = 1.3118^{+0.0056}_{-0.0053} R_\odot$). Both the stars in KIC65 are very much solar-like ($R_{Aa} = 1.0719^{+0.0019}_{-0.0020} R_\odot$ and $R_{Ab} = 1.0101^{+0.0017}_{-0.0014} R_\odot$). A quick look at the MCMC corner plots (Fig. 5) tells us that the uncertainty on radii measurements is mostly affected by degeneracy in L_{Aa} which is itself degenerate with l_3 . The e_A is adopted to be zero for both systems. But the MCMC maps show shifts of 2σ and 3σ from zero, for BD44 (Fig.5) and KIC65 (Fig.6) respectively. This small eccentricity can possibly be induced in the LC due to spots

¹² We followed the process of adding tides as explained in: https://github.com/dtamayo/reboundx/blob/master/ipython_examples/TidesConstantTimeLag.ipynb

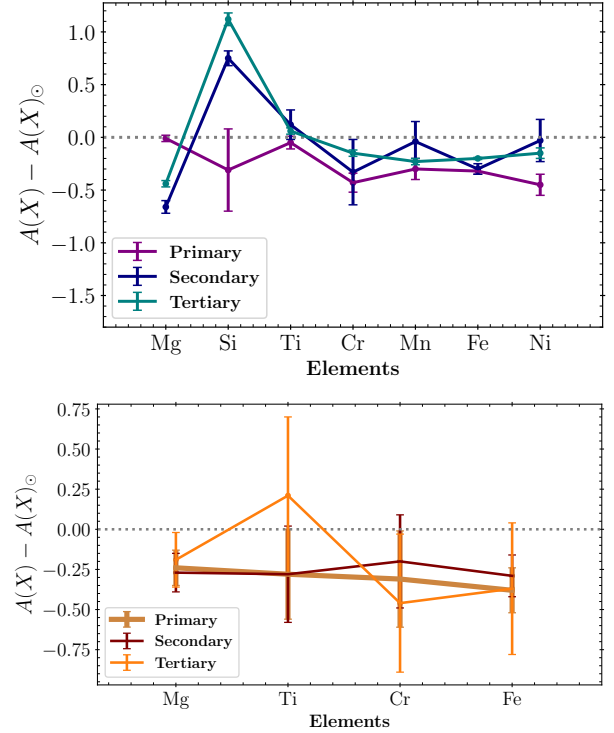


Figure 8. Abundance variation for all three stars in BD44 (top) and KIC65 (bottom). The plotted abundances are relative to solar abundances, which is denoted by the dotted line.

or be due to perturbations from the tertiary star. Unfortunately with current observations, it is difficult to decouple these effects.

The temperatures of the BD44 binary stars are lower ($T_{Aa}^{\text{eff}} = 5822 \pm 202K$ and $T_{Ab}^{\text{eff}} = 5449 \pm 100K$) compared to those of KIC65 ($T_{Aa}^{\text{eff}} = 6490 \pm 129K$ and $T_{Ab}^{\text{eff}} = 6397 \pm 123K$). While the similar temperatures of KIC65Aa and KIC65Ab can explain the similar eclipse depths, we expect a temperature ratio of 0.772 (compared to 0.936 from the spectral analysis) from the LC fitting of BD44. This discrepancy can arise due to the cold spots in BD44, which affect the spectroscopic temperature measurement.

The stars in BD44 have quite different $v\sin(i)$ with the BD44Aa having a value of 23.21 km s^{-1} compared to 39.60 km s^{-1} for BD44Ab. KIC65 has similar $v\sin(i)$ for the stars in the inner binary as expected from stars with similar radii. But when comparing with calculated synchronised velocities, we find that the observed velocities are larger than expected. The $v\sin(i)$ of the tertiary of KIC65 and BD44 are similar.

Both KIC65 and BD44 are metal-poor systems having $[M/H] -0.28 \pm 0.22$ and -0.24 ± 0.21 respectively. While most of the stars are found to be α -enhanced systems, BD44Ab and BD44B were the only stars with negative α . We calculated the abundances of some elements whose lines showed up on the spectra. We compare the abundances (see Tables 2 and 3) for all three stars, in both the systems, in Fig.8. While all the stars in KIC65 have similar abundances (within error bars), BD44Ab and BD44B have a rise in $A(\text{Si})$ and a dip in $A(\text{Mg})$ compared to BD44Aa (Fig.8). The total set of all parameters is given in Table. 1 for comparison.

Table 1. All adopted parameters for BD44 and KIC65 (except i_m). Unsymmetrical errors correspond to uncertainties estimated using MCMC sampling.

	BD +44 2258			KIC 06525196		
Orbital Parameters						
	Aa–Ab	A–B		Aa–Ab	A–B	
t_0 [BJD - 2450000]	8740.8268426			2421.6563579		
P [days]	3.4726217 ± 0.0000015			$3.42059774 \pm 0.00000014$		
a [R_\odot]	12.06 ± 0.12			12.053 ± 0.018		
e	0.000^a			0.000^a		
i [deg]	$80.1271^{+0.0084}_{-0.0057}$			$84.7083^{+0.0051}_{-0.0063}$		
ω [deg]	–			–		
q	1.074 ± 0.021			0.9383 ± 0.0026		
K_1 [km s^{-1}]	89.66 ± 0.98			85.96 ± 0.12		
K_2 [km s^{-1}]	83.47 ± 1.37			91.62 ± 0.12		
Stellar and atmospheric parameters						
	Aa	Ab	B	Aa	Ab	B
Flux fraction (from Spectroscopy)	0.3758 ± 0.0268	0.5139 ± 0.0285	0.1104 ± 0.0088	0.4851 ± 0.0225	0.4010 ± 0.0154	0.1139 ± 0.0181
Flux fraction (from Photometry)	$0.4021^{+0.0039}_{-0.0030}$	$0.5101^{+0.0021}_{-0.0031}$	$0.0878^{+0.0016}_{-0.0015}$	$0.4990^{+0.0101}_{-0.0084}$	$0.4060^{+0.0051}_{-0.0068}$	$0.0950^{+0.0033}_{-0.0034}$
M [M_\odot]	0.941 ± 0.033	1.011 ± 0.029	0.907 ± 0.065	1.0351 ± 0.0055	0.9712 ± 0.0039	0.777 ± 0.012
R [R_\odot]	$1.3118^{+0.0056}_{-0.0053}$	$2.4387^{+0.0035}_{-0.0048}$	$1.67^{+0.70}_{-0.59}$	$1.0719^{+0.0020}_{-0.0019}$	$1.0101^{+0.0014}_{-0.0017}$	$0.74^{+0.80}_{-0.38}$
T_{eff} [K]	5822 ± 202	5449 ± 100	5261 ± 181	6490 ± 129	6397 ± 123	5393 ± 319
$\log(g)$ [dex]	4.19^b	3.69^b	3.95 ± 0.39	4.39^b	4.41^b	4.58 ± 0.63
v_{mic} [km s^{-1}]	2.36 ± 0.75	1.78^c	1.19 ± 0.5	1.39 ± 0.54	1.18 ± 0.53	1.5^c
v_{mac} [km s^{-1}] ^c	4.69	3.76	3.43	9.28	8.43	5.94
$v \sin(i)$ [km s^{-1}]	23.21 ± 2.19	39.60 ± 3.26	5.34 ± 1.41	20.69 ± 1.45	18.39 ± 1.15	5.23 ± 1.34
α [dex]	0.21 ± 0.12	-0.22 ± 0.08	-0.21 ± 0.11	0.07 ± 0.11	0.16 ± 0.11	0.29 ± 0.24
System parameters						
$\log(\text{age})$ [dex]	$9.89^{+0.03}_{-0.05}$			9.49 ± 0.06		
$[M/H]_{\text{ISpec}}$ [dex]	-0.24 ± 0.21			-0.28 ± 0.22		
$[Fe/H]_{\text{ISpec}}$ [dex]	$-0.40^{+0.15}_{-0.10}$			$-0.45^{+0.15}_{-0.35}$		
$E(B - V)^d$ [mag]	$0.176^{+0.019}_{-0.049}$			$0.053^{+0.040}_{-0.030}$		
Distance ^d [pc]	$194.5^{+3.3}_{-10.3}$			$220.01^{+2.26}_{-1.68}$		

^a Fixed while optimisation. ^b Fixed from LC fitting solutions. ^c Obtained from empirical tables. ^d Based on isochrone fitting.

Table 2. Abundances of individual elements of the components of BD44. Solar abundances are presented for comparison (Asplund et al. 2009).

Elements	Primary	Secondary	Tertiary	Solar
¹² Mg	7.59 ± 0.03	6.94 ± 0.06	7.16 ± 0.03	7.60 ± 0.04
¹⁴ Si	7.20 ± 0.39	8.26 ± 0.07	8.63 ± 0.06	7.51 ± 0.03
²² Ti	4.90 ± 0.06	5.25 ± 0.14	5.01 ± 0.03	4.95 ± 0.05
²⁴ Cr	5.21 ± 0.09	5.31 ± 0.31	5.49 ± 0.03	5.64 ± 0.04
²⁵ Mn	5.13 ± 0.10	5.39 ± 0.19	5.20 ± 0.03	5.43 ± 0.05
²⁶ Fe	7.18 ± 0.03	7.20 ± 0.05	7.30 ± 0.01	7.50 ± 0.04
²⁸ Ni	5.77 ± 0.10	6.19 ± 0.20	6.07 ± 0.05	6.22 ± 0.04

Table 3. Abundances of individual elements of the components of KIC65.

Elements	Primary	Secondary	Tertiary	Solar
¹² Mg	7.36 ± 0.11	7.33 ± 0.12	7.41 ± 0.17	7.60 ± 0.04
²² Ti	4.67 ± 0.28	4.67 ± 0.30	5.16 ± 0.49	4.95 ± 0.05
²⁴ Cr	5.33 ± 0.30	5.44 ± 0.29	5.17 ± 0.43	5.64 ± 0.04
²⁶ Fe	7.12 ± 0.14	7.21 ± 0.13	7.13 ± 0.41	7.50 ± 0.04

4.2 Physical parameters of the Tertiary

The tertiary stars orbit the inner binary with the periods of 254.84 ± 0.05 and 418.0 ± 0.4 d for BD44 and KIC65, respectively. They are different in both mass and radius. The mass of the tertiary in BD44 is close to solar ($0.907 \pm 0.065 M_\odot$) while tertiary of KIC65 is less massive ($0.777 \pm 0.012 M_\odot$). The estimated radii have large errors, but a comprehensive look at all the signatures suggests that

the tertiary in BD44 has an inflated atmosphere and therefore a radius larger than one expected for a main-sequence star of this mass. The tertiary of KIC65 is most likely to have a radius of $0.74 R_\odot$. The stars themselves are orbiting with different periods around the inner binary system. The tertiary of BD44 is in an orbit with higher eccentricity ($e_{AB} = 0.598$) than KIC65 ($e_{AB} \sim 0.3$; Fig. 9). These different configurations will mostly affect the timescale of secular perturbations which depend on e_{AB} (Ford et al. 2000).

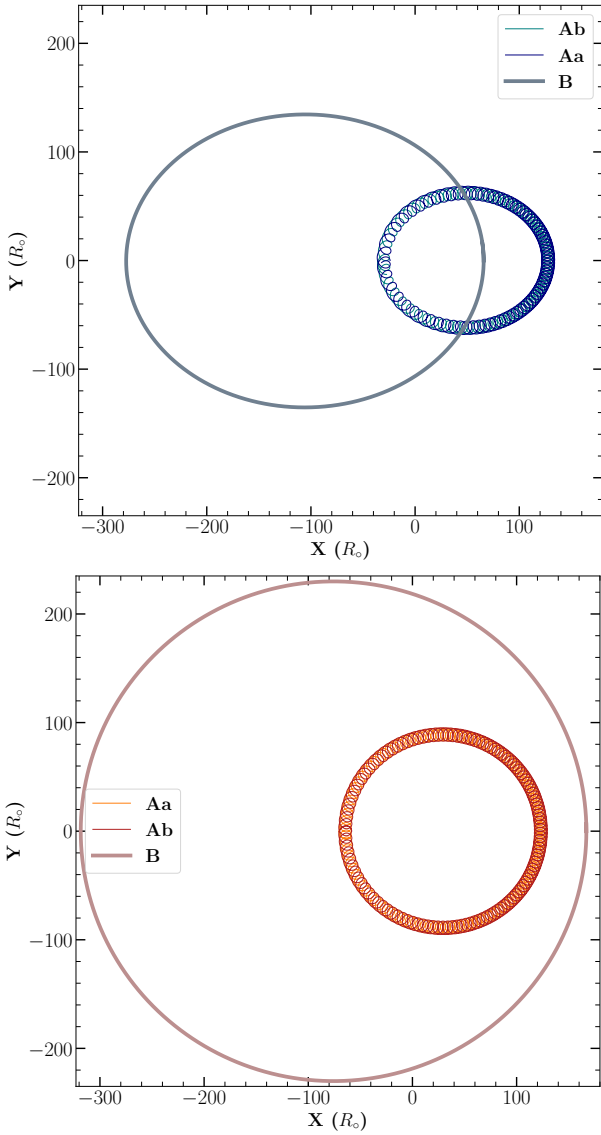


Figure 9. Orbital path of all the stars of BD44 (top) and KIC65 (bottom). The orbits are viewed perpendicular to the orbital plane of the inner binary (for $i_m = 4^\circ$) and are integrated over one outer-orbit period.

4.3 Possible Mutual Inclinations

Short-term numerical integration gave us an estimate of inclination changes of the inner binary (Δi_A) for different values of Ω_{AB} . We then obtained observed Δi_A by using inclination values obtained by Helminiak et al. (2017) for KIC65, subtracted from the values obtained in this work. While for BD44 we used the inclinations observed in Sector-16 and Sector-49 of *TESS* LCs (Table.4). This gave us possible values of Ω_{AB} for the observed Δi_A (Fig.10). We then used Eq.(4) to translate the possible Ω_{AB} values to possible i_m values for all possible configurations (Table.5).

4.4 Age and Evolution

Isochrone fitting puts the $\log(\text{age})$ for BD44 between 9.84 and 9.92 (95% confidence level), for metallicity range of -0.25 to -0.50 dex. The formally best fit was found for $\log(\text{age}) = 9.89$ (7.8 Gyr) and $[\text{Fe}/\text{H}] = -0.40$ dex. While the primary of BD44, BD44Aa, is a main-

Table 4. Variation of i_A over time.

System	Initial i_A [deg]	Final i_A [deg]	Time (yrs)
BD44	80.1271 ± 0.008	80.1521 ± 0.017	2.7
KIC65	85.15 ± 0.34	84.7083 ± 0.005	6.9

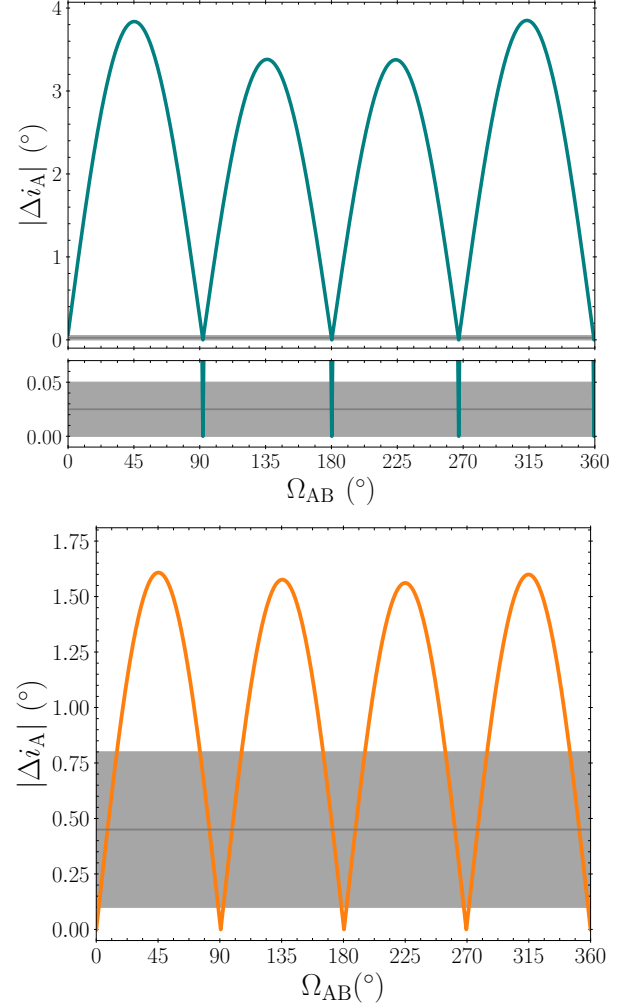


Figure 10. Variation of $|\Delta i_A|$ from numerical simulations for different values of Ω_{AB} , for BD44 (top) and KIC65 (bottom). The timescale of the simulation corresponds to the length of the available LCs. The grey lines show the observed $|\Delta i_A|$ with the shaded regions representing the errors in measurements. The overlapping regions represent the possible values of Ω_{AB} . The lower panel of the top figure represents a zoomed-in view of the observed variations.

sequence star, BD44Ab is a sub-giant. With the large uncertainties in the parameters of BD44B, it is hard to determine its evolutionary state. But the simultaneous mass-radius and mass-temperature isochrone fit depicts it as a sub-giant star (Fig.11). The other signatures of BD44B being a sub-giant are found in (i) large amplitude of BF (Fig.2), and (ii) similar abundances (Fig.8) as that of the BD44Aa (which is a sub-giant itself). However, with the available data, we can not completely rule out the possibility that it is a main-sequence star, less massive and smaller than the primary.

The isochrone-based, reddening-free distance was found to be

Table 5. Estimates of mutual inclination for possible values of Ω_{AB} .

System	Ω_{AB}	i_m	
		Config.A	Config.B
BD44	359.46 ± 0.76	4.03 ± 0.10	175.97 ± 0.01
	266.97 ± 0.79	90.56 ± 0.76	89.45 ± 0.76
	180.23 ± 0.83	156.27 ± 0.01	23.73 ± 0.01
	92.16 ± 0.80	89.71 ± 0.77	90.29 ± 0.77
KIC65	353.80 ± 4.85	6.18 ± 4.83	173.82 ± 4.83
	269.41 ± 11.12	90.09 ± 11.02	89.91 ± 11.02
	180.42 ± 11.18	164.60 ± 0.30	15.40 ± 0.30
	90.67 ± 11.10	90.16 ± 11.00	89.83 ± 11.00
	6.19 ± 4.85	6.17 ± 4.83	173.83 ± 4.83

194.5 pc, which is significantly larger than the GDR3 Part 3 value of 165.8 ± 0.6 pc. The distribution of acceptable models is very skewed, and none of the acceptable models reached a distance lower than 184 pc. The tension is probably caused by the tertiary, which was formally found to be less massive but seemingly more evolved than the primary. Its parameters could probably be better determined with additional observations around the outer orbit's pericenter, where the tertiary's RVs reach their minimum. It should also be noted that the GDR3 solution is of worse quality than for KIC65.

Even though having the binary stars with masses similar to BD44, both the primary and secondary of KIC65 are main-sequence stars along with its tertiary. This immediately suggests that KIC65 is significantly younger than BD44. The fitting procedure for KIC65 resulted in $\log(\text{age}) = 9.49$ (3.1 Gyr) and $[\text{Fe}/\text{H}] = -0.45$ dex, with the 95% confidence level ranges of 9.43 to 9.55, and -0.80 to -0.30 dex, respectively. The isochrone-based reddening-free distance ($\sim 220 \pm 2$ pc) is in excellent agreement with, and of comparable precision to, the GDR3 solution for an astrometric binary model (222.3 ± 1.7 pc), even when it was not used as a constraint.

4.5 Dynamical Evolution

Long-term evolution of KIC65 shows that the system is stable for 600 Myrs more. But BD44 becomes a binary system within 550 Myrs due to the collision/merger of the inner binary. This collision will be driven by increasing tidal forces due to the increasing radius of the sub-giant BD44Ab (Fig.12: upper-panel). The radius of the star will exceed the Roche-limit (Eggleton 1983) at around 450 Myr and will drive the merger process unless the formation of a contact binary stabilises this system. This merger is mostly due to the tides in the inner binary as a lack of tertiary companion would have only delayed the merger by a few Myrs (Fig.12: lower-panel) for most of the estimated i_m . But a i_m near 90° will make the system merge faster (< 400 Myr) than the lower values of i_m (Fig.13).

4.6 Spot Evolution

The light curve of BD44 is highly varying over different sectors owing to the migrating and evolving cold spots. The activity of BD44 is corroborated by its ultraviolet and X-ray emissions. The distortions on the BF's of the stars in BD44 indicate the secondary (BD44Ab) to have more spots. The occurrence of the fast-evolving and migrating spots is common on sub-giant stars. The biggest spot on the secondary is still visible in the newest Sector-49 of *TESS*

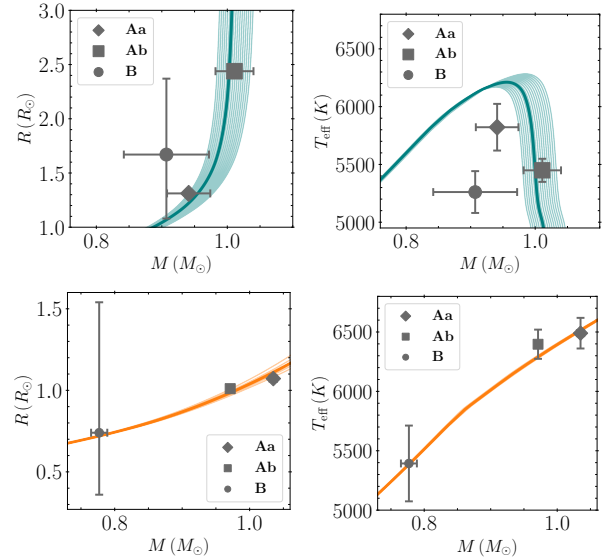


Figure 11. Mass-Radius (left column) and Mass-Temperature (right column) isochrone fits for BD44 (top; in green) and KIC65 (bottom; in orange). The shaded area represents the parameter-space corresponding to the errors of the fitting. The respective measurements from the stars are plotted in grey. The size of the points are relative to their radii.

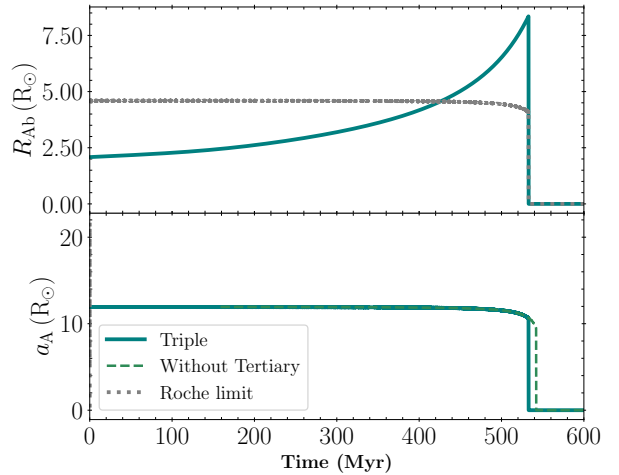


Figure 12. Variation of the radius of BD44Ab and the semi-major axis of the inner binary of BD44 as simulated in REBOUNDX for $i_m = 4^\circ$. The radius variation is interpolated from MIST grids. The grey dotted line in the top panel shows Roche-limit for the system. The dashed line in the lower panel shows the change in the collision time if no tertiary star was present.

observations. This enabled us to study its migration. We used spot parameters obtained from LC fitting using PHOEBE 2, from different sectors, to quantify the migration (see Table 6). Using the values of longitudes and the mid-times of the first primary eclipse (T_{seg}) for each segment, we calculated the rate of change of the longitude. We found that the spot moves $\sim 0.696^\circ$ per orbital cycle of the inner binary. The spot moves from a longitude of $0^\circ - 180^\circ$ in 2.5 years. Extrapolating this, we get a spot migration period of 5 years. The migration is most probably caused by differential rotation because the spot in question is near the poles, as seen in low c^{spot} values (Fig.14). Petit et al. (2004) represents the differential rotation as,

$$\Omega(c^{\text{spot}}) = \Omega_{\text{eq}} - \Delta\Omega \cos^2(c^{\text{spot}}) \quad (10)$$

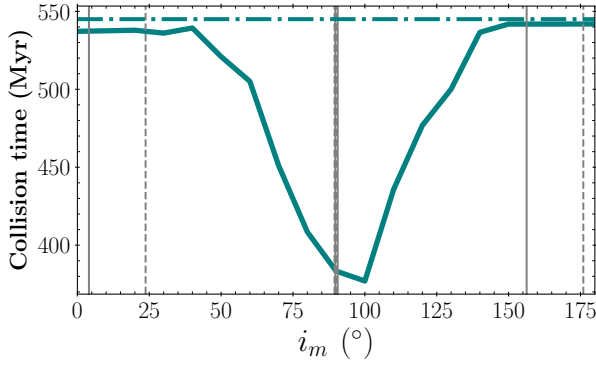


Figure 13. The simulated collision time of the inner binary of BD44 for different mutual inclinations. The green dot-dashed line shows the time for collision without a tertiary companion. The vertical grey lines represent the possible values of i_m . Solid lines represent possible i_m for Config.A while dashed lines are for Config.B.

Table 6. Spot parameters for the coldest spot on the secondary of BD44. The parameters have been obtained for each sector using PHOEBE 2 modelling.

Parameters	S16	S22	S49
T_{seg} [BJD-2457000]	1740.8270	1900.5753	2640.2640
$r_{\text{Ab}}^{\text{spot}}$ [deg]	42.846	37.311	39.611
$T_{\text{Ab}}^{\text{spot}}$	0.8988	0.9296	0.8500
$c_{\text{Ab}}^{\text{spot}}$ [deg]	22.000	35.745	21.913
$l_{\text{Ab}}^{\text{spot}}$ [deg]	0.000	29.975	180.233

where, Ω is the differential rotation as a function of co-latitude (or latitude), Ω_{eq} is the rotation at the equator, and $\Delta\Omega$ is the difference in rotation rate between the pole and the equator. Calculating an estimate of $\Delta\Omega$ in BD44Ab gives us $\Delta\Omega = 0.0044 \pm 0.0004 \text{ rad d}^{-1}$. This small differential rotation has been seen in the K1 sub-giant primary in the RS CVn system HR 1099 (Petit et al. 2004) and also K-type main-sequence of V471 Tau (Hussain et al. 2006) with $\Delta\Omega = 0.0152 \pm 0.0008 \text{ rad d}^{-1}$ and $\Delta\Omega = 0.0016 \pm 0.0060 \text{ rad d}^{-1}$ respectively.

5 CONCLUSIONS

We obtained independent measurements of different parameters for two triple-lined CHT. Using LC modelling, RV modelling, and SPD followed by spectral analysis, we obtained stellar, orbital and atmospheric parameters of all the six stars in the two CHT. A multi-parameter isochrone fitting constrained the ages of the two systems to be in the order of Gyrs. Isochrones, along with abundances obtained from the disentangled spectra, helped us classify the evolutionary state of the tertiary in the two systems. Furthermore, we gathered the following information about the two systems:

- **KIC65:** The period-ratio of the CHT is ≈ 122 . All stars in the system are main-sequence stars. The system is a metal-poor one and is α -enhanced. The tertiary has 5 possible configurations of mutual inclination with a possibility of near co-planar orbit. Due to the comparatively smaller mass of the tertiary and a wider orbit, the system is stable in the long-term for all values of mutual inclinations.

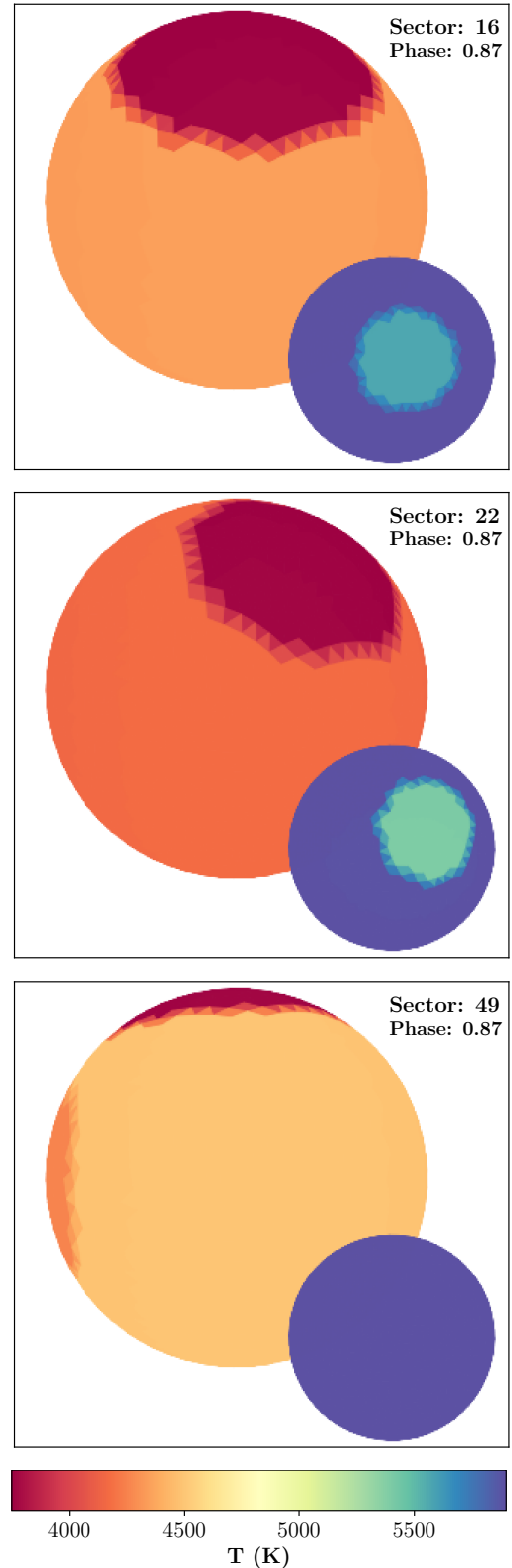


Figure 14. Spot positions on the inner binary stars of BD44 (at the same phase) for Sector-16 (top), Sector-22 (middle), and Sector-49 (bottom) as obtained with PHOEBE 2 modelling. The stable-spot near the pole of the secondary is the spot that affects the eclipse depths the most and is the one that migrates with a timescale of ~ 5 yr.

The distance estimated in our study is consistent with the distance obtained in Gaia-DR3.

- **BD44:** This system is a relatively tighter CHT with a period-ratio ≈ 73 . But still, this system is well above the dynamical instability¹³ limit as defined in [Mardling & Aarseth \(2001\)](#). The system consists of one main-sequence star (almost at the turn-off) and two sub-giant stars. The abundance patterns of the two sub-giants are similar while the main-sequence differs in Mg and Si abundances. The system has large and cold spots which affect the measurement of some of our parameters. But using the spots we were able to calculate a differential rotation in the sub-giant of the inner binary. This sub-giant component of the inner pair also contributes significantly to tidal forces. Numerical simulations with tidal interactions show that the inner binary will collide/merge in a few hundred of Myrs due to the radius of the sub-giant exceeding the Roche limit. This leaves behind a wide binary unless the formation of a contact binary stabilises the system. The tertiary does hasten this merger but the effects are drastic if the tertiary is orbiting in an orbit perpendicular to the inner binary orbit.

Both the targets can benefit from further photometric and spectroscopic observations which will improve the estimate of obtained parameters. The photometric observations themselves will be quite crucial to check for inclination variations of the inner binary and therefore will give better constraints on the mutual inclination. This will be helpful in constraining evolution scenarios of the CHT as well as star-formation scenarios of these close triples. Nevertheless, this study shows that the use of parameters obtained using independent observations is crucial for the realistic modelling of CHT.

ACKNOWLEDGEMENTS

The authors thank the referee for the invaluable comments and suggestions. The authors thank Dr. Kyle Conroy and Dr. Andrej Prša for their valuable suggestions and help with PHOEBE 2. The authors also acknowledge Dr. Hanno Rein for his help in setting up REBOUND simulations. This work is funded by the Polish National Science Centre (NCN) through grant 2021/41/N/ST9/02746. A.M., F.M., T.P., and M.K. are supported by NCN through grant no. 2017/27/B/ST9/02727. F.M. gratefully acknowledges support from the NASA TESS Guest Investigator grant 80NSSC22K0180 (PI A. Prša). This paper includes data collected with the TESS mission, obtained from the Mikulski Archive for Space Telescopes (MAST) data archive at the Space Telescope Science Institute (STScI). Funding for the TESS mission is provided by the NASA Explorer Program. STScI is operated by the Association of Universities for Research in Astronomy, Inc., under NASA contract NAS 5–26555. This work also presents results from the European Space Agency (ESA) space mission Gaia. Gaia data are being processed by the Gaia Data Processing and Analysis Consortium (DPAC). Funding for the DPAC is provided by national institutions, in particular, the institutions participating in the Gaia MultiLateral Agreement (MLA).

DATA AVAILABILITY

The *TESS* data used in this article are public and hosted on MAST. The data can be accessed from <http://dx.doi.org/10.17909/>

[fp8v-5705](#). The spectroscopic data will be made available upon request.

REFERENCES

- Akashi M., Soker N., 2017, *MNRAS*, **469**, 3296
 Asplund M., Grevesse N., Sauval A. J., Scott P., 2009, *ARA&A*, **47**, 481
 Bianchi L., Herald J., Efremova B., Girardi L., Zabot A., Marigo P., Conti A., Shiao B., 2011, *Ap&SS*, **335**, 161
 Blanco-Cuaresma S., 2019, *MNRAS*, **486**, 2075
 Blanco-Cuaresma S., Soubiran C., Heiter U., Jofré P., 2014, *A&A*, **569**, A111
 Borkovits T., 2022, *Galaxies*, **10**, 9
 Borkovits T., Rappaport S., Hajdu T., Sztakovics J., 2015, *MNRAS*, **448**, 946
 Borkovits T., Hajdu T., Sztakovics J., Rappaport S., Levine A., Bíró I. B., Klagyivik P., 2016, *MNRAS*, **455**, 4136
 Borkovits T., Rappaport S. A., Hajdu T., Maxted P. F. L., Pál A., Forgács-Dajka E., Klagyivik P., Mitnyan T., 2020, *MNRAS*, **493**, 5005
 Borkovits T., Rappaport S. A., Toonen S., Moe M., Mitnyan T., Csányi I., 2022, *Monthly Notices of the Royal Astronomical Society*
 Box G. E. P., Jenkins G. M., 1976, in *Holden-Day Series in Time Series Analysis*.
 Cardelli J. A., Clayton G. C., Mathis J. S., 1989, *ApJ*, **345**, 245
 Choi J., Dotter A., Conroy C., Cantiello M., Paxton B., Johnson B. D., 2016, *ApJ*, **823**, 102
 Claret A., Bloemen S., 2011, *A&A*, **529**, A75
 Conroy K. E., et al., 2020, *ApJS*, **250**, 34
 Dotter A., 2016, *ApJS*, **222**, 8
 Duchêne G., Kraus A., 2013, *ARA&A*, **51**, 269
 Eggleton P. P., 1983, *ApJ*, **268**, 368
 Eggleton P. P., Kiseleva-Eggleton L., 2001, *ApJ*, **562**, 1012
 Eggleton P. P., Verbunt F., 1986, *MNRAS*, **220**, 13P
 Eisner N. L., et al., 2022, *MNRAS*, **511**, 4710
 Ford E. B., Kozinsky B., Rasio F. A., 2000, *ApJ*, **535**, 385
 Foreman-Mackey D., Hogg D. W., Lang D., Goodman J., 2013, *PASP*, **125**, 306
 Foreman-Mackey D., et al., 2019, *The Journal of Open Source Software*, **4**, 1864
 Francq C., Zakoian J.-M., 2009, *Journal of Time Series Analysis*, **30**, 449
 Fuller J., Dekeris A., Borkovits T., Huber D., Bedding T. R., Kiss L. L., 2013, *MNRAS*, **429**, 2425
 Gaia Collaboration et al., 2022, arXiv e-prints, p. arXiv:2208.00211
 Gilmore G., et al., 2012, *The Messenger*, **147**, 25
 Gray D. F., 2005, *The Observation and Analysis of Stellar Photospheres*. Cambridge University Press
 Grevesse N., Asplund M., Sauval A. J., 2007, *Space Sci. Rev.*, **130**, 105
 Gronchi G. F., Tommei G., 2007, *Discrete and Continuous Dynamical Systems - B*, **7**, 755
 Gustafsson B., Edvardsson B., Eriksson K., Jørgensen U. G., Nordlund Å., Plez B., 2008, *A&A*, **486**, 951
 Hadrava P., 1995, *A&AS*, **114**, 393
 Hamers A. S., Dosopoulou F., 2019, *ApJ*, **872**, 119
 Helminiak K. G., Ukita N., Kambe E., Kozłowski S. K., Sybilski P., Ratajczak M., Maehara H., Konacki M., 2016, *MNRAS*, **461**, 2896
 Helminiak K. G., et al., 2017, *MNRAS*, **468**, 1726
 Helminiak K. G., et al., 2021, *MNRAS*, **508**, 5687
 Holmgren D. E., Hadrava P., Harmanec P., Eenens P., Corral L. J., Yang S., Ak H., Bozič H., 1999, *A&A*, **345**, 855
 Horvat M., Conroy K. E., Pablo H., Hambleton K. M., Kochoska A., Giannmarco J., Prša A., 2018, *ApJS*, **237**, 26
 Howell S. B., et al., 2014, *PASP*, **126**, 398
 Hussain G. A. J., Allende Prieto C., Saar S. H., Still M., 2006, *MNRAS*, **367**, 1699
 Hut P., 1981, *A&A*, **99**, 126
 Ilijic S., Hensberge H., Pavlovski K., Freyhammer L. M., 2004, in *Hilditch R. W., Hensberge H., Pavlovski K., eds, Astronomical Society of the Pacific Conference Series Vol. 318, Spectroscopically and Spatially Resolving the Components of the Close Binary Stars*. pp 111–113

¹³ This limit is derived for prograde co-planar motion.

Izumiura H., 1999, in Chen P. S., ed., Proc. 4th East Asian Meeting on Astronomy, Observational Astrophysics in Asia and its Future. Kunming Yunnan Observatory, p. 77

Jones D., Pejcha O., Corradi R. L. M., 2019, *MNRAS*, 489, 2195

Jones D., et al., 2020, *ApJS*, 247, 63

Kambe E., et al., 2013, *PASJ*, 65, 15

Kervella P., Thévenin F., Di Folco E., Ségransan D., 2004, *A&A*, 426, 297

Kobulnicky H. A., Fryer C. L., 2007, *ApJ*, 670, 747

Konacki M., Muterspaugh M. W., Kulkarni S. R., Helminiak K. G., 2010, *ApJ*, 719, 1293

Korth J., Moharana A., Pešta M., Czavalinga D. R., Conroy K. E., 2021, *Contributions of the Astronomical Observatory Skalnaté Pleso*, 51, 58

Kozai Y., 1962, *AJ*, 67, 591

Lee A. T., Offner S. S. R., Kratter K. M., Smullen R. A., Li P. S., 2019, *ApJ*, 887, 3352

Lidov M. L., 1962, *Planet. Space Sci.*, 9, 719

Maoz D., Mannucci F., Nelemans G., 2014, *ARA&A*, 52, 107

Marcadon F., Helminiak K. G., Marques J. P., Pawlaszek R., Sybilski P., Kozłowski S. K., Ratajczak M., Konacki M., 2020, *MNRAS*, 499, 3019

Mardling R. A., Aarseth S. J., 2001, *MNRAS*, 321, 398

Mason B. D., Hartkopf W. I., Gies D. R., Henry T. J., Helsel J. W., 2009, *AJ*, 137, 3358

Maxted P. F. L., et al., 2020, *MNRAS*, 498, 332

Mayer P., Harmanec P., Pavlovski K., 2013, *A&A*, 550, A2

Moe M., Kratter K. M., 2018, *ApJ*, 854, 44

Naoz S., Fabrycky D. C., 2014, *ApJ*, 793, 137

Nelder J. A., Mead R., 1965, *The Computer Journal*, 7, 308

Paxton B., Bildsten L., Dotter A., Herwig F., Lesaffre P., Timmes F., 2011, *ApJS*, 192, 3

Paxton B., et al., 2013, *ApJS*, 208, 4

Paxton B., et al., 2015, *ApJS*, 220, 15

Paxton B., et al., 2018, *ApJS*, 234, 34

Perets H. B., Fabrycky D. C., 2009, *ApJ*, 697, 1048

Petit P., et al., 2004, *MNRAS*, 348, 1175

Prša A., et al., 2016, *ApJS*, 227, 29

Raghavan D., et al., 2010, *ApJS*, 190, 1

Randich S., Gilmore G., Gaia-ESO Consortium 2013, *The Messenger*, 154, 47

Rappaport S., Deck K., Levine A., Borkovits T., Carter J., El Mellah I., Sanchis-Ojeda R., Kalomeni B., 2013, *ApJ*, 768, 33

Rappaport S. A., et al., 2022, *MNRAS*, 513, 4341

Rein H., Liu S. F., 2012, *A&A*, 537, A128

Rein H., Tamayo D., 2015, *MNRAS*, 452, 376

Ricker G. R., et al., 2015, *Journal of Astronomical Telescopes, Instruments, and Systems*, 1, 014003

Rucinski S., 1999a, *Turkish Journal of Physics*, 23, 271

Rucinski S., 1999b, in Hearnshaw J. B., Scarfe C. D., eds, *Astronomical Society of the Pacific Conference Series Vol. 185, IAU Colloq. 170: Precise Stellar Radial Velocities*. p. 82 ([arXiv:astro-ph/9807327](https://arxiv.org/abs/astro-ph/9807327))

Shatsky N., Tokovinin A., 2002, *A&A*, 382, 92

Simon K. P., Sturm E., 1994, *A&A*, 281, 286

Tamayo D., Rein H., Shi P., Hernandez D. M., 2020, *MNRAS*, 491, 2885

Tokovinin A., 2004, in Allen C., Scarfe C., eds, *Revista Mexicana de Astronomía y Astrofísica Conference Series Vol. 21, Revista Mexicana de Astronomía y Astrofísica Conference Series*. pp 7–14

Tokovinin A., 2017, *ApJ*, 844, 103

Tokovinin A., 2021, *Universe*, 7, 352

Tokovinin A., 2022, *ApJ*, 926, 1

Toonen S., Portegies Zwart S., Hamers A. S., Bandopadhyay D., 2020, *A&A*, 640, A16

Torres G., Andersen J., Giménez A., 2010, *A&ARv*, 18, 67

Voges W., et al., 1999, *A&A*, 349, 389

Zasche P., Paschke A., 2012, *A&A*, 542, L23

Zasche P., Vokrouhlický D., Barlow B. N., Mašek M., 2023, *The Astronomical Journal*, 165, 81

Zucker S., Mazeh T., 1994, *ApJ*, 420, 806

von Zeipel H., 1910, *Astronomische Nachrichten*, 183, 345

APPENDIX A: DISTANCE AND REDDENING ESTIMATES FROM THE ISOCHRONES

The reddening-free distance d_0 are estimated simultaneously with the reddening $E(B - V)$, using the available observed total magnitudes in different filters, and the predicted total brightness of the system in the same filters, for a given triplet of points (= stellar masses) on the same isochrone. We use the T_{eff} -surface brightness relations from Kervella et al. (2004), to calculate the distances d_λ and distance moduli $(m - M)_\lambda = 5 \log(d_\lambda) + 5$ in each band. To obtain the extinction-free modulus $(m - M)_0$ we fit a straight line on the A_λ vs. $(m - M)_\lambda$ plane, where the A_λ are extinction coefficients in each band. We followed the extinction law of Cardelli et al. (1989) $A_U : A_B : A_V : A_R : A_I : A_J : A_H : A_K = 4.855 : 4.064 : 3.1 : 2.545 : 1.801 : 0.88 : 0.558 : 0.36$, which assumes $R_V = 3.1$. The slope of the fitted line in this approach is the reddening $E(B - V)$, while the intercept is the extinction-free modulus $(m - M)_0$, which can be translated into the distance d_0 . In the isochrone fitting process, where the distance is used as one of the constraints, the reproduced d_0 value is the one that is being compared with d .

APPENDIX B: RADIAL VELOCITIES

The RVs for BD44, extracted using TODCOR method, are given in Table.B1.

APPENDIX C: SPOT PARAMETERS

The PHOEBE2 model for BD44 included one spot on the Aa star and two on the Ab star. While we considered the most stable spot (spot-2 on Ab) for our calculations of differential rotation, the other parameters are important while modelling the LC and are given in Table.C1. The spot parameters vary over the three *TESS* sectors: Sector-16 (S16), Sector-22 (S22), and Sector-49 (S49).

APPENDIX D: BF FITTING TABLES

The BF fitting was done on multiple spectra of different epochs. Though the profile of every fit was similar, the flux fraction of each component varied slightly, which was necessary to consider while spectral disentangling. This variation was noticed for $v \sin(i)$ too but their variations were not significant to consider during spectral analysis. The complete tables for these parameters are available in the online version.

This paper has been typeset from a \LaTeX file prepared by the author.

Table B1. RV measurements of BD44.

BJD-2450000	v_1 ($km\ s^{-1}$)	ϵ_1 ($km\ s^{-1}$)	v_2 ($km\ s^{-1}$)	ϵ_2 ($km\ s^{-1}$)	γ ($km\ s^{-1}$)	ϵ_γ ($km\ s^{-1}$)	v_3 ($km\ s^{-1}$)	ϵ_3 ($km\ s^{-1}$)
7022.350624	-21.499	0.697	-146.291	0.505	-81.664	0.754	-78.406	0.079
7061.170892	13.564	0.428	-149.393	0.973	-65.001	0.956	-106.205	0.100
7062.263807	—	—	-3.669	0.863	—	—	—	—
7110.041913	-22.493	0.471	-139.493	0.394	-78.901	0.654	-78.143	0.075
7111.161334	-160.274	0.578	3.675	0.355	-81.230	0.878	-76.942	0.086
7142.999934	-148.156	0.714	-23.570	0.426	-88.090	0.746	-63.215	0.083
7144.008005	-13.377	0.565	-161.962	1.019	-85.013	0.929	-62.731	0.135
7148.097089	-16.490	1.381	-160.184	0.379	-85.768	1.023	-62.282	0.077
7490.046763	-164.541	1.803	-2.964	0.496	-86.641	1.250	-68.064	0.227
7526.015228	-10.156	2.387	-159.806	0.391	-82.306	1.452	-76.503	0.095
7528.026002	-164.479	1.040	7.485	0.497	-81.571	1.032	-77.027	0.140
7530.053976	-13.474	1.193	-154.691	0.526	-81.558	0.965	-78.010	0.087
7539.052136	—	—	-41.870	0.339	—	—	—	—
7540.110845	3.205	0.606	-166.138	0.514	-78.439	0.925	-82.127	0.123
7755.261393	-6.755	0.688	-164.869	0.429	-82.985	0.881	-69.878	0.103
7813.057543	-146.164	2.782	2.688	0.778	-74.399	1.660	-92.769	0.105
7813.175027	-137.988	1.525	-8.703	0.446	-75.657	1.037	—	—
7814.125822	-3.179	1.464	-141.592	0.745	-69.911	1.081	-93.820	0.093
7816.093416	-150.858	2.080	12.322	0.828	-72.185	1.402	-95.491	0.128
7816.322403	-152.826	2.013	13.918	0.420	-72.435	1.343	-95.617	0.126
7846.107080	16.267	1.456	-123.088	0.526	-50.919	1.051	-139.779	0.231
7891.177386	-14.944	1.876	-163.681	0.491	-86.653	1.240	-66.297	0.118
7892.950768	-152.526	0.821	-12.576	0.450	-85.053	0.839	-66.027	0.078
7894.027357	—	—	-154.775	0.303	—	—	—	—
7950.023399	-3.531	0.670	-173.935	0.750	-85.687	0.978	-62.241	0.097
7954.983416	-164.296	0.700	-3.259	0.266	-86.656	0.882	-62.650	0.101
8066.362164	-156.728	2.378	14.806	0.152	-74.028	1.496	-91.838	0.117

Table C1. Spot parameters for spots on primary (Aa) and secondary (Ab) of BD44.

Parameters	S16	S22	S49
T_{Aa}^{spot}	0.9535	0.9362	1.04848
T_{Ab}^{spot1}	0.9922	0.9806	0.9545
T_{Ab}^{spot2}	0.8988	0.9296	0.8499
r_{Aa}^{spot} [deg]	29.449	29.846	33.943
r_{Ab}^{spot1} [deg]	31.9971	30.446	11.390
r_{Ab}^{spot2} [deg]	42.846	37.311	39.611
c_{Aa}^{spot} [deg]	80.735	69.893	80.735
c_{Ab}^{spot1} [deg]	90.977	89.047	90.977
c_{Ab}^{spot2} [deg]	22.000	35.745	21.913
i_{Aa}^{spot} [deg]	180.000	194.891	84.0973
i_{Ab}^{spot1} [deg]	162.488	196.044	262.305
i_{Ab}^{spot2} [deg]	0.000	29.975	180.233